International Journal of Fatigue 198 (2025) 109008

Contents lists available at ScienceDirect

International Journal of Fatigue

journal homepage: www.elsevier.com/locate/ijfatigue

Fatigue crack growth of untreated and heat-treated WAAM ER70S-6 carbon steel☆

Mariela Mendez-Morales [a,*], Joel S. Jesus [b], Ricardo Branco [b], Trayana Tankova [c], Carlos Rebelo [a]

[a] University of Coimbra, ISISE, ARISE, Department of Civil Engineering, Rua Luis Reis Santos, 3030-790 Coimbra, Portugal
[b] University of Coimbra, CEMMPRE, ARISE, Department of Mechanical Engineering, Rua Luis Reis Santos, 3030-788 Coimbra, Portugal
[c] Delft University of Technology, Department of Engineering Structures, Stevinweg 1, 2628 CN Delft, the Netherlands

ARTICLE INFO

Keywords:
Fatigue crack growth
Plasticity-induced crack closure
Additive manufacturing
WAAM ER70S-6 carbon steel

ABSTRACT

The paper addresses the fatigue crack growth behaviour of untreated and heat-treated WAAM ER70S-6 carbon steel. Specimens were extracted from the printed wall along different directions (vertical and horizontal) and tested under mode-I loading at two stress ratios ($R = 0.05$ and $R = 0.25$). Crack closure was measured using Digital Image Correlation (DIC). The microstructure of the untreated material mainly consisted of polygonal ferrite and intergranular lamellar pearlite. After heat treatment, pearlite decomposed, allowing ferrite to grow and reducing hardness. The load ratio influenced fatigue crack growth rates due to variations in crack closure levels. However, the loading direction relative to the print layer orientation did not significantly affect the crack growth rate. Fracture surfaces were examined by scanning electron microscopy to identify the main fatigue crack growth mechanisms associated with the different loading orientations and material conditions. Fractographic analysis revealed a mixed fracture mechanism, characterised by cleavage in the harder pearlite-rich regions and fatigue crack propagation striations in the softer ferrite-dominant areas. Minor manufacturing defects, such as inclusions and porosity, were also observed. The tested WAAM carbon steel exhibited slightly lower performance than conventional steels of a similar grade, aligning closely with the existing literature for WAAM ER70S-6 carbon steel.

1. Introduction

Despite the systematic study of wire-arc additive manufacturing (WAAM) carbon steel in recent years [1–3], the unique characteristics of this material have hindered the full comprehension of its mechanical behaviour, especially under cyclic loading. Nevertheless, if WAAM continues to grow at the rate experienced in the last years in the construction sector, understanding the fatigue behaviour of WAAM carbon steel is imperative [4–6].

WAAM carbon steel, like conventional welding, inherently contains internal defects [7,8] and surface undulations [9,10], making it susceptible to fatigue failure. Under such conditions, the fatigue crack propagation stage often becomes the dominant phase of the fatigue process. Thus, accurate evaluation of the fatigue crack growth (FCG) rate is critical for effectively assessing the structural integrity of WAAM carbon steel structures.

The FCG behaviour of WAAM metallic materials has already been studied [11–14]. However, research on WAAM carbon steel remains limited. Ermakova et al. [15] studied the effect of specimen orientation on the FCG behaviour of WAAM ER70S-6 steel produced using an oscillatory deposition pattern. Their findings indicated that the extraction location relative to the WAAM wall had little influence on FCG behaviour. However, vertical specimens were more sensitive to material inhomogeneities and exhibited brittle fracture characteristics. Compared to heat-affected zone S355 steels, the WAAM specimens showed higher FCG rates, although the results remained close to the upper bound of the FCG data for S355G8 + M base metal.

Shamir et al. [16] further investigated the impact of sample location and orientation on FCG behaviour, concluding that neither factor significantly affected FCG rates. This study also compared the parallel deposition pattern with the oscillatory pattern studied by Ermakova et al. [15], finding similar FCG behaviour between both strategies in the

☆ This article is part of a special issue entitled: 'Fatigue at VHCF9' published in International Journal of Fatigue.

* Corresponding author.
E-mail address: mendezmorales@dec.uc.pt (M. Mendez-Morales).

https://doi.org/10.1016/j.ijfatigue.2025.109008
Received 27 December 2024; Received in revised form 10 March 2025; Accepted 17 April 2025
Available online 18 April 2025

intermediate stress-intensity factor range (ΔK) region. Additionally, Ermakova et al. [17] examined the effect of rolling and laser shock peening surface treatment techniques on FCG and residual stress distribution on WAAM ER70S-6 and ER100S-1 carbon steel. In the samples fabricated using ER70S-6 wire, both surface treatment techniques improved fatigue performance by reducing the FCG rates in the treated areas compared to untreated samples.

More recently, Huang et al. [18] conducted a comprehensive analysis of WAAM ER70S-6 carbon steel, examining various fabrication strategies and orientations, and compared the results with data from conventional and WAAM-produced steels in the literature. The study found that WAAM specimens exhibited FCG behaviour similar to conventionally produced steels, with no significant anisotropy observed in the material.

The previous studies have significantly advanced the understanding of FCG behaviour in WAAM ER70S-6 steel. Nevertheless, the effect of stress ratio (R) on FCG rates for different printing orientations in the Paris regime remains unexplored. The stress ratio can also affect crack closure, i.e. the contact of crack surfaces before the minimum applied load is reached [19]. Crack closure is generally induced by wake plasticity, the presence of oxides, or the roughness of fracture surfaces. However, at both intermediate and high ΔK values, plasticity-induced crack closure (PICC) is the predominant mechanism. In contrast, oxide-induced crack closure (OICC) and roughness-induced crack closure (RICC) are more relevant at low ΔK values, particularly near the threshold region. PICC can significantly reduce the effective stress-intensity factor range (ΔK_{eff}), delaying the intrinsic mechanisms that drive the crack growth [20]. Therefore, accurate predictions of fatigue crack propagation life require a careful characterisation of PICC [21], which may involve accurate calculations of several critical parameters, such as crack-tip opening stress and variations in compliance during the loading and unloading phases of the fatigue cycle [22].

The layer-by-layer deposition approach of WAAM generates residual stresses due to the complex thermal cycles and the rapid cooling rates inherent to this additive manufacturing process [23]. These residual stresses, which are typically compressive near the substrate and tensile in the upper layers, can directly influence the effective stress-intensity factor range and, consequently, the fatigue crack propagation lifetime [17]. Post-processing heat treatments, such as stress relief, annealing, normalisation or tempering, can be applied to carbon steel to reduce residual stresses and promote microstructure refinement, enhancing FCG resistance [24]. Nevertheless, so far, there is a lack of investigations addressing the effect of post-processing heat treatments on FCG of WAAM ER70S-6 steel.

In summary, while previous research has advanced the understanding of FCG in WAAM metals, key aspects remain insufficiently explored for ER70S-6 carbon steel, a material widely used in structural engineering. Specifically, the influence of stress ratio on crack closure mechanisms, the effect of printing orientation, and the role of post-processing heat treatments require further investigation. This study addresses these gaps by examining the FCG behaviour of WAAM-produced ER70S-6 carbon steel under different stress ratios ($R = 0.05$ and $R = 0.25$) and printing orientations (horizontal and vertical) in both untreated and annealed conditions.

Furthermore, the study systematically compares untreated and annealed specimens, with the results evaluated against existing data for both WAAM-produced and conventionally manufactured steels. Microstructural characterisation and hardness profiling were performed to assess material properties, while scanning electron microscopy (SEM) was employed to examine fracture surfaces and identify the predominant crack growth mechanisms. Overall, this research enhances the predictive accuracy of fatigue life models and provides new insights into the FCG behaviour of WAAM-produced carbon steel. The findings of this study contribute to the integration of WAAM technology in the design of structural components where FCG is a concern, while also providing a comparison with conventional steels and established design standards, ultimately supporting the wider adoption of WAAM-produced steels in fatigue-sensitive applications.

2. Experimental procedure

2.1. WAAM material

The feedstock material used in this research was low-carbon steel AWS A5.18 ER70S-6/ISO 14341 – A – G 42 4M21 G 3Si1 copper-coated wire of 1.0 mm diameter, hereafter referred to as ER70S-6. Table 1 summarises the nominal chemical composition as a weight percentage [25], while Table 2 lists its main mechanical properties according to the manufacturer [26].

The fatigue specimens were extracted from a carbon steel wall produced at the AM Construction Laboratory of the University of Coimbra. The wall was manufactured using an ABB IRB 4600 robot in combination with a CMT Fronius TPS 400i welding machine. The fabrication parameters given in Table 3 were selected to match those used by Tankova et al. [27] and Mendez-Morales et al. [28], ensuring continuity to the work carried out by this research group. The total printing time for the wall, including the time the torch was off, was slightly over two hours. The calibrated layer height was 2.52 mm.

Fig. 1 illustrates the selected printing direction corresponding to a parallel deposition trajectory and the schematic fabrication setup. The beads were deposited in an alternating parallel pattern per layer in both transverse and vertical directions. Since no pre-heating was applied to the substrate material, the first layers of printed material were discarded to avoid any heterogeneities and ensure that the specimens were extracted after the production temperature stabilised, as shown in Fig. 1. Further details on the material production are available in the works of Tankova et al. [27] and Mendez-Morales et al. [28].

2.2. Specimen geometry

To investigate the influence of the printing strategy on the FCG behaviour of WAAM carbon steel, the wall geometry was designed to allow the extraction of three C(T) specimens in the X-direction, as shown in Fig. 2(a). Moreover, specimens were extracted in two orientations: horizontal (H) and vertical (V) (see Fig. 1). Horizontal specimens were cut along the Y-direction, parallel to the deposition trajectory, while vertical specimens were extracted along the Z-direction, perpendicular to the deposition trajectory. One specimen on each orientation, marked in red in Fig. 2(b), was selected for heat treatment (HT) to investigate potential improvements in FCG behaviour. A previous study conducted by the authors concluded that through-thickness variations had no significant influence on the microstructure or fatigue performance of the studied WAAM carbon steel for this printing strategy [28]. Furthermore, milling three coupons from the same volume enables the analysis of material that has reached a steady-state condition.

The geometry of the C(T) specimens was defined per ASTM E647-24 [29], as illustrated in Fig. 2(b), with a thickness, B, of 6 mm, a width, W, of 36 mm, and a notch length, a_0, of 16 mm. One face of each C(T) specimen was polished using a Struers LaboPol-5 machine, employing a series of sandpapers with progressively finer grits: P180, P320, P600,

Table 1
Chemical composition of ER70S-6 feedstock wire (wt.%).

Feedstock wire ER70S-6			
C	0.06 – 0.15	**P**	0.025 max.
Mn	1.40 – 1.85	**S**	0.035 max.
Cr	0.15 max.	**Si**	0.80 – 1.15
Ni	0.15 max.	**Cu**	0.50 max.
Mo	0.15 max.	**Fe**	Bal.
V	0.03 max.		

Table 2
Mechanical properties of ER70S-6 feedstock wire.

Feedstock wire	Yield strength (MPa)	Ultimate tensile strength (MPa)
ER70S-6	420	520

Table 3
CMT-WAAM wall fabrication parameters.

Process parameter	Detail	Process parameter	Detail
Current (A)	155	Robot speed (mm/s)	10.0
Voltage (V)	15.7	Shielding gas	98 % Ar + 2 % CO_2 (M12)
Wire diameter (m/min)	1.0	Dwell time (s)	15
Wire feed (m/min)	6.0	Layer height (mm)	2.44

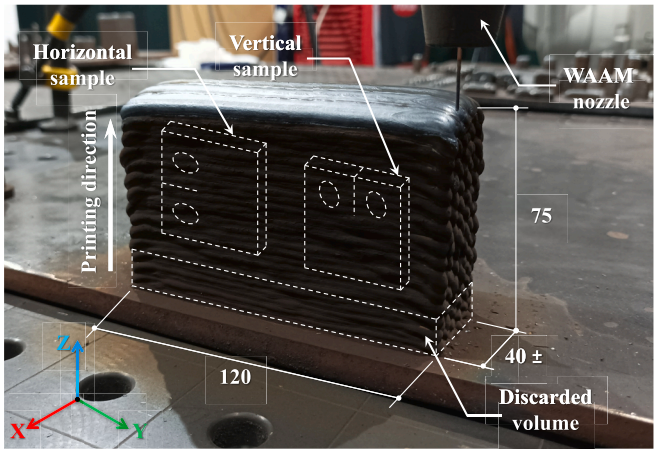

Fig. 1. Schematic AM Construction Lab setup and indication of horizontal and vertical orientations of the C(T) specimens (no scale, dimensions in millimetres).

and P1200. A 3 μm diamond paste was subsequently applied to achieve a mirror-like finish to remove any residual surface scratches. The opposite face of the specimens was coated with a water-based white paint and dried. A fine speckle pattern was then applied using an Iwata airbrush. This speckle pattern is critical for collecting precise data on the displacement field at the crack tip under varying loads, utilising Digital Image Correlation (DIC) techniques used here to measure crack closure.

2.3. Post-processing heat treatment

The annealing heat treatment involved heating the specimens to 800 °C at 10 °C/min, followed by a first cooling stage down to 400 °C at the same rate. This was followed by a second cooling stage, which went down to 100 °C at 5 °C/min, and finally, cooling to room temperature in open air. According to Nemani et al. [30], heat treatments of low alloy steels can be classified based on the austenitising temperature as upper-critical (for temperatures above Ac_3 line of Fe-Fe_3C binary phase diagram) or intercritical (between Ac_1 and Ac_3 lines). The critical temperatures Ac_1 and Ac_3 can be calculated based on the alloying elements, as shown below:

$$Ac_1(^\circ\mathrm{C}) = 723 - 10.7Mn - 3.9Ni + 29Si + 16.7Cr + 290As + 6.38W \quad (1)$$

$$Ac_3(^\circ\mathrm{C}) = 910 - 230(C)^{0.5} - 15.2Ni + 44.7Si + 10.4V + 31.5Mo + 13.1W \quad (2)$$

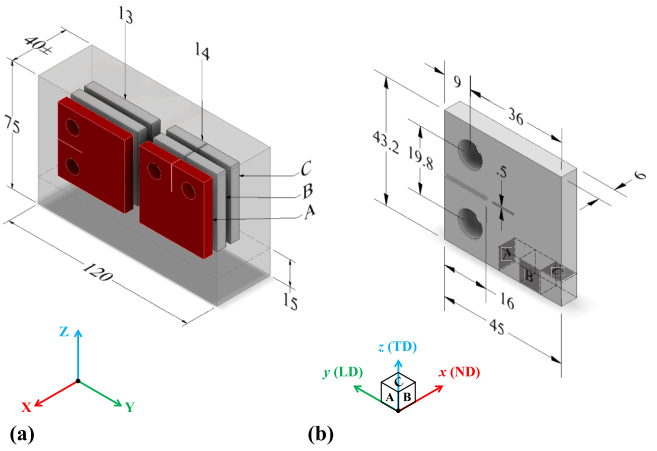

Fig. 2. (a) Wall's geometry for C(T) specimens (no scale, dimensions in millimetres); and (b) C(T) specimen geometry with microstructure extraction locations (no scale, dimensions in millimetres).

Based on the chemical composition of the feedstock wire, as detailed in Table 1, Ac_1 is calculated to be 705.12 °C and Ac_3 is 826.48 °C. The selected temperatures for the heat treatment were intentionally kept below Ac_3 to achieve an annealing microstructure.

2.4. Microstructure characterisation and hardness evaluation

Microstructure characterisation and hardness evaluation were performed to better understand the effects of printing orientation and post-processing heat treatment on the FCG behaviour of the tested WAAM carbon steel.

Microstructure characterisation was carried out following the guidelines outlined in the ASTM E3-11 [31] standard. The analysis encompassed two untreated specimens: one cut horizontally (H-13C) and another cut vertically (V-14C), and two heat-treated (HT) specimens: one cut horizontally (H-13A) and another cut vertically (V-14A). The metallographic samples were extracted from the C(T) specimens along three orthogonal planes aligned with the longitudinal direction (LD), transverse direction (TD), and normal direction (ND) direction, see Fig. 2(b). The metallographic samples were polished to a surface finish of 1 μm and then were etched with 5 % Nital solution. After that, the microstructure features were observed using a Leica DM 4000 M LED optical microscope.

Hardness evaluation was conducted on the same specimens used for microstructure characterisation (H-13C, V-14C, H-13A (HT), V-14A) along the same orthogonal planes (LD, TD, and ND; see Fig. 2(b)). The testing procedure was performed in accordance with E384-22 standard [32]. A load of 0.50 kgf was applied and held for 15 s using a Struers Duramin microhardness tester equipped with a Vickers indenter. Five random indentations were performed for each sample.

2.5. Fatigue crack growth testing

Fatigue crack propagation tests were conducted following ASTM E647-24 [29] under load-controlled conditions at a cyclic frequency of 10 Hz and room temperature. Six C(T) specimens were tested under two different load ratios: $R = 0.05$ (specimens H-13C, V-14A, and V-14C; see Fig. 2(a)) and $R = 0.25$, (specimens H-13A (HT), H-13B, and V-14B; see Fig. 2(a)). H-13A (HT) and V-14A were heat-treated while the others were tested in the untreated condition.

A fatigue pre-crack was introduced into the specimens as recommended by the standard, employing a stress-intensity factor range (ΔK) of 15 MPa$\sqrt{m}$, derived from previous research on the same material performed by Huang et al. [18]. Based on this ΔK and the defined load ratios, the load amplitude (ΔP) was calculated following the standard by

solving Eq. (3) [29]:

$$\Delta K = \frac{\Delta P}{B\sqrt{W}} \bullet \frac{(2+\alpha)}{(1-\alpha)^{\frac{3}{2}}} \bullet (0.886 + 4.64\alpha - 13.32\alpha^2 + 14.72\alpha^3 - 5.6\alpha^4) \tag{3}$$

where B is the thickness, W is the width, and $\alpha = a/W$ is the normalised crack length. This last expression is valid for $a/W \geq 0.2$, and a represents the crack length measured from the load application point to the tip of the crack. For the geometry of the C(T) specimen of this research, Eq. (3) yields $\Delta P = 4.05\ kN$ for $R = 0.05$ ($P_{max} = 4.26\ kN$ and $P_{min} = 0.21\ kN$) and $\Delta P = 4.00\ kN$ for $R = 0.25$ ($P_{max} = 5.33\ kN$ and $P_{min} = 1.33\ kN$).

The experimental setup consisted of an Instron ElectroPuls E10000 machine with a dynamic compression/tension load capacity of ±10 kN coupled with a Specwell 8.5° Wide Extra Short Focus spotting lens with 45× magnification and a Mitutoyo micrometre, enabling crack lengths measurement every 0.20 mm using an optical measurement methodology. Additionally, a 41-megapixel Hayer microscopic camera was employed for more accurate data acquisition.

DIC was used to monitor fatigue crack growth and assess crack closure based on full-field strain tensor data [33,34]. Crack propagation measurement started after an initial 2.0 mm crack extension, with subsequent measurements taken at 1 mm intervals. Each measurement involved a 3-minute recording period with the microscopic camera, during which the load cycled from minimum to maximum. The recordings were later converted into 180 images (one image per second) using *DVDVideoSoft* software [35]. This data was subsequently processed with *GOM Correlate* software [36], where a digital extensometer with a gauge length of 0.15 mm ± 0.02 mm was used to measure displacement at a distance of 0.25 mm ± 0.02 mm from the crack tip. Each image provided a corresponding measurement of crack displacement, which was correlated with the load value at that specific time. The resultant data was used to plot the crack length, a, as a function of the number of cycles, N. The test concluded with the rupture of the specimen.

The crack closure was determined by calculating the fraction of the load cycle during which the crack remains fully closed, the so-called U parameter, defined as follows:

$$U = \frac{P_{max} - P_{op}}{P_{max} - P_{min}} \tag{4}$$

where P_{max} and P_{min} represent maximum and minimum loads, respectively, and P_{op} is the crack opening load. P_{op} was calculated by identifying the point where the least square correlation coefficient reaches its maximum value [37]. The process begins by calculating the correlation coefficient for the upper 10 % of the load–displacement ($P-\delta$) data. Then, the next $P-\delta$ point is incrementally added, and the correlation coefficient is recalculated. The procedure is repeated until the entire data set is analysed. The crack opening load is defined as the load corresponding to the maximum correlation coefficient. The methodology used to identify U and P_{op} was based on the procedure proposed by Allison et al. [38], implemented in a previous study conducted by this research group [39].

2.6. SEM examination of fracture mechanisms

After the FCG tests, the fracture surfaces were examined to investigate the fracture mechanisms of the Paris regime associated with the different material orientations (vertical and horizontal) and material conditions (untreated and heat-treated). Firstly, the samples were cut via a high-speed cutting machine and cleaned in an ultrasonic bath. The SEM analysis was carried out using a Hitachi SU3800 model and encompassed the six tested cases.

3. Results and discussion

3.1. Microstructure and hardness

The metallographic analysis obtained from the three orthogonal planes (A, B, and C) can be observed in Fig. 3. In general, all samples showed a microstructure characteristic of low-carbon steel consisting of a ferrite matrix with a secondary pearlite phase [40]. Fig. 3(a) shows the microstructure of the H-13C samples as a representative example of the as-build condition, indicating that the sample direction did not significantly influence the microstructure. The average grain size, considering equiaxial grains, ranged from 3 μm to 18 μm. In contrast, the microstructure of the heat-treated samples H-13A and V-14A, shown in Fig. 3 (b) and (c), exhibited coarser grains compared to the untreated condition. The average grain size increased from 8 μm to 25 μm, indicating that heat treatment resulted in grain growth.

The increase in grain size observed in ferrite-pearlite steel during annealing at 800 °C can be attributed to microstructural evolution of the material caused by heat exposure. At this temperature, several key microstructural processes contribute to grain growth. At 800 °C, the steel is within the temperature range that promotes recovery and recrystallisation. The high temperature causes atomic diffusion, allowing atoms in the crystal lattice to move more freely. This diffusion reduces dislocations and other defects within the crystal structure. As the dislocations are removed, grain boundaries face less resistance, leading grains to grow.

In ferrite-pearlite steels, the pearlite phase, which is composed of alternating layers of ferrite and cementite, plays an essential role in limiting grain growth. However, as annealing progresses and temperature increases, the pearlite begins to break down, and the cementite may decompose or redistribute. This further facilitates the growth of the ferrite grains, which are the softer phase of the steel. The phenomenon of grain growth is thermodynamically driven by the reduction in energy associated with the presence of grain boundaries. Smaller grains have more grain boundaries, which corresponds to higher energy in the system. As the grains grow, the total grain boundary area relative to the total area decreases, reducing the system's overall energy. In summary, the increase in grain size during annealing of ferrite-pearlite steel at 800 °C occurs due to atomic diffusion, decomposition of pearlite, and the natural tendency of the material to minimise internal energy. The result is a coarser grain structure, which can influence the mechanical properties of the steel, such as its strength due to loss of hardness.

As described previously, at 800 °C, the steel undergoes a partial transformation where the pearlite begins to break down. Ferrite, being a relatively soft phase, becomes more prominent as cementite decomposes or redistributes. This leads to a decrease in hardness, as ferrite is much softer than pearlite or cementite phases. Additionally, the annealing process allows residual stresses introduced during WAAM to relax, further contributing to the softening of the material. While the microstructure becomes more uniform during annealing, the lack of hard phases, such as cementite, reduces the overall hardness of the steel. The reduction in hardness is a typical outcome of annealing, as it is a heat treatment designed to improve ductility and machinability, rather than maintain high hardness. In conclusion, the decrease in hardness of ferrite-pearlite steel annealed at 800 °C is primarily due to the transformation and redistribution of phases, especially the reduction of cementite content and the increased proportion of softer ferrite.

The average hardness values obtained from the five random measurements performed on the three orthogonal planes (A, B, and C) of the C(T) specimens, see Fig. 2(b), are summarised in Table 4. The hardness of the untreated material was higher than that of the heat-treated. In addition, the heat-treated specimens exhibited uniform hardness irrespective of the orientation. In contrast, the untreated samples exhibited some material anisotropy, with the vertical specimen showing the highest hardness value. Overall, the hardness measurements of the untreated condition, particularly those obtained for the V14-C specimen,

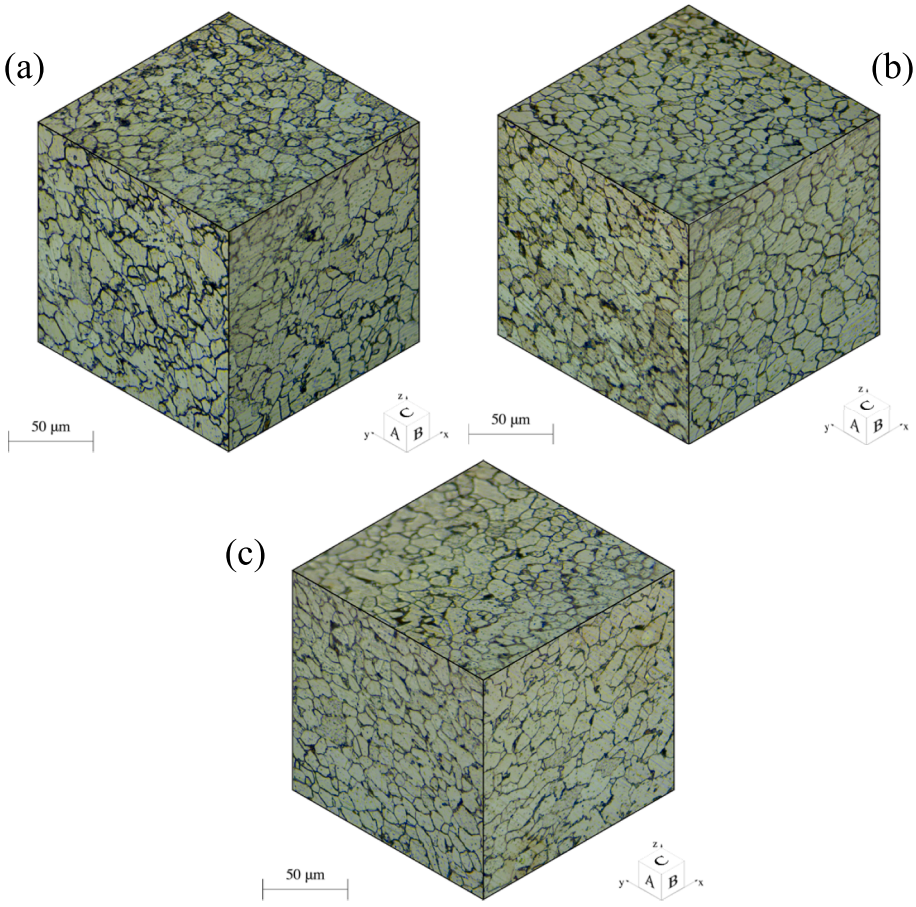

Fig. 3. Isometric micrographs of metallographic samples: (a) untreated H-13C, (b) heat-treated H-13A, and (c) heat-treated V-14A.

Table 4
Vickers hardness of the WAAM ER70S-6 carbon steel.

Specimen	Plane A	Plane B	Plane C	Average
H-13C	146	144	149	146
V-14C	149	173	155	159
H-13A (HT)	139	132	141	137
V-14A (HT)	130	139	141	137
Ermakova et al. [41]				158
Huang et al. [18]*				161
S355 steel, Dantas et al. [42]				152

* 10 kgf load indenter; the others were tested using 0.5 kgf.

are consistent with the values reported by other authors for WAAM ER70S-6 carbon steel. The variations relative to the previous studies, based on the average hardness of the vertical specimen, are lower than 1 %. Similarly, compared to conventional steel, such as S355 steel, the measured hardness is relatively close, with a variation lower than 5 %.

3.2. Fatigue crack growth behaviour

Fig. 4 presents the data obtained from the FCG tests, illustrating crack length, a, as a function of the number of cycles, N. This representation facilitates a comparative analysis of the behaviour of the tested specimens. As expected, the lower stress ratio ($R = 0.05$) exhibit shorter crack lengths for the same number of cycles at the higher stress ratio ($R = 0.25$). This outcome aligns with existing literature on the effect of stress ratio on FCG behaviour [43–45].

For instance, at a crack length of 10 mm, the fatigue crack propagation life of the horizontal specimens (represented by the red data sets in Fig. 4) increases by a factor of 4.6 when the stress ratio is reduced

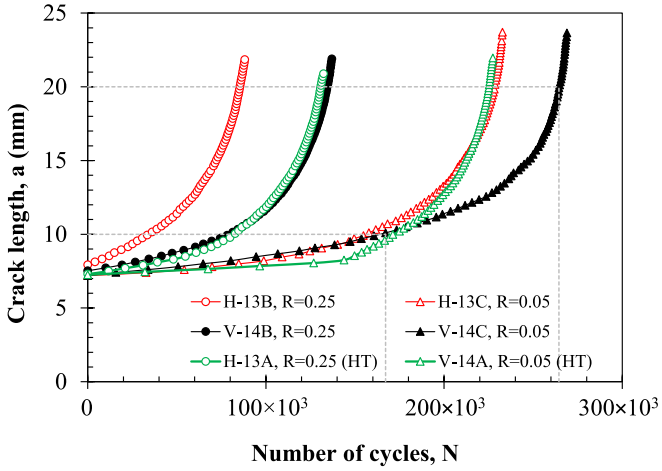

Fig. 4. Crack length versus number of loading cycles for horizontal and vertical specimens tested at $R = 0.25$ and $R = 0.05$ (reference crack lengths in dashed grey lines).

from 0.25 to 0.05. However, as the crack propagates, this effect weakens; at a crack length of 20 mm, the fatigue crack propagation life increases by a factor of 2.7. In contrast, vertical specimens (represented by the black data sets in Fig. 4) show less variation with changes in stress ratio, with fatigue life increasing by factors of 2.1 and 2.0 for crack lengths of 10 mm and 20 mm, respectively.

Additionally, vertical specimens demonstrate superior resistance to fatigue crack propagation than horizontal specimens, regardless of the

stress ratio. Using the reference crack lengths of 10 mm and 20 mm, at a stress ratio of 0.25 (represented by rounded markers in Fig. 4), vertical specimens' fatigue crack propagation life improves by factors of 2.3 and 1.6, respectively. At a stress ratio of 0.05 (represented by triangular markers), the enhancement in fatigue crack propagation life for vertical specimens is approximately 1.1 and 1.2 times for crack lengths of 10 mm and 20 mm, respectively. These preliminary results suggest that, despite vertical specimens showing a superior resistance, the influence of this effect on fatigue crack propagation life is reduced at lower stress ratios.

Overall, specimen H-13B, tested at $R = 0.25$, shows the most detrimental case, characterised by the largest crack length for a given number of cycles. Conversely, specimen V-14C, tested at $R = 0.05$, exhibits the highest resistance to fatigue crack propagation. Based on these results alone, the effect of heat treatment on the FCG behaviour remains inconclusive.

The curves showing the variation of crack growth rate with stress-intensity factor ($da/dN - \Delta K$) were derived from Fig. 4 using the 5-point polynomial method. This method, recommended by international standards for scenarios involving increasing stress-intensity factor amplitude, was employed to calculate da/dN [29]. Furthermore, Eq. (3) was used to compute ΔK. Fig. 5 presents these results (i.e. da/dN versus ΔK) on a log–log scale, categorised by the specimen orientation relative to the deposition direction. Note that coupons labelled as HT underwent heat treatment.

For the horizontal specimens, see Fig. 5(a), where the crack propagates parallel to the welding beads, the specimen tested at $R = 0.05$ (H-13C) exhibited lower propagation velocities for the same ΔK value compared to the specimens tested at $R = 0.25$ in the same orientation (H-13A and H-13B), indicating superior resistance to fatigue crack propagation. This is expected from the literature and attributed to the initially higher crack closure phenomenon at lower R values. Additionally, for ΔK values ranging from 24 MPa$\sqrt{m}$ to 28 MPa$\sqrt{m}$, this specimen shows a significant variation in the curve trend, possibly due to material imperfections or a finer microstructure. Specimens H-13B and H-13A (HT), tested at $R = 0.25$, displayed similar trends in their fatigue crack propagation rate, suggesting that heat treatment did not enhance the material's performance.

For vertical specimens, shown in Fig. 5(b), where the crack propagates perpendicular to the welding beads, there is also no visible improvement in the crack resistance of specimen V-14A (HT), tested at $R = 0.05$, after heat treatment, likely due to the loss of hardness post-heat treatment being more influential than the differences in respective crack closures. Comparing the two specimens tested at the same R ratio, i.e. $R = 0.05$, V-14C and V-14A (HT), reinforces that heat treatment was not beneficial, as there is a considerable difference between their $da/dN - \Delta K$ curves at equal stress ratio, especially at lower values of ΔK. The curves tend to converge at ΔK values over 35 MPa$\sqrt{m}$, when the crack approaches rupture.

Fig. 6 shows the $da/dN - \Delta K$ curves, organised by stress ratio, allowing for a clear assessment of the influence of printing orientation. For $R = 0.05$, as displayed in Fig. 6(a), specimen V-14C slower propagation up to a stress-intensity factor range of approximately 30 MPa$\sqrt{m}$. This may be attributed to the greater hardness and finer microstructure of the specimen, providing higher resistance to fatigue crack propagation. Beyond this ΔK value, the trend of the vertical specimen curve closely follows that of the horizontal sample H-13C. Moreover, the propagation velocity of the heat-treated specimen is the highest of all, hinting that the selected heat treatment had no beneficial effect on the FCG response of the material.

The minor differences in FCG resistance at a stress ratio of 0.05 in favour of the vertical coupons may be due to the tortuous path the crack must navigate when propagating perpendicular to the welding beads; this explanation has been suggested by previous scholars on the behaviour of WAAM Ti-6Al-4V alloy [46,47]. Nevertheless, these differences may also be attributed to tensile residual stresses or PICC, which will be investigated in the following section.

Fig. 6(b) shows the $da/dN - \Delta K$ curves for a stress ratio $R = 0.25$ for the two orientations studied. In this second stress-ratio scenario, all three samples display nearly identical FCG performance with little scatter. This suggests that the hardness-induced resistance to propagation observed in the V-14C specimen, tested at $R = 0.05$, is insufficient to slow fatigue crack propagation at higher loading ratios. Furthermore, crack closure is almost negligible because, at higher minimum loads, the crack remains fully open longer during a load cycle. Similar results in which the crack growth rate and scatter were dependent on the loading have been found by earlier investigations [15].

3.3. Plasticity-induced crack closure

As previously mentioned, the crack closure phenomenon in fatigue crack propagation refers to the partial or complete contact between the crack faces during part of the loading cycle, even when the applied load is not zero. This contact reduces the effective stress-intensity factor range (ΔK_{eff}) experienced by the crack tip, thereby slowing down the crack growth rate. The plastic deformation at the crack tip during previous loading cycles can result in residual deformation, causing the crack faces to come into contact during unloading. This mechanism is known as PICC.

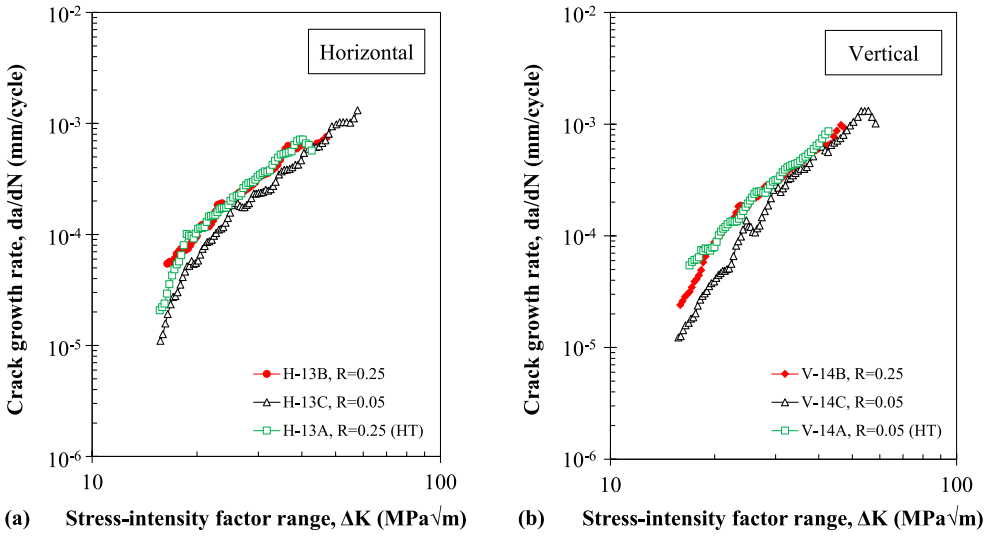

Fig. 5. Fatigue crack growth rate against stress-intensity factor range organised per orientation: (a) horizontal specimens and (b) vertical specimens.

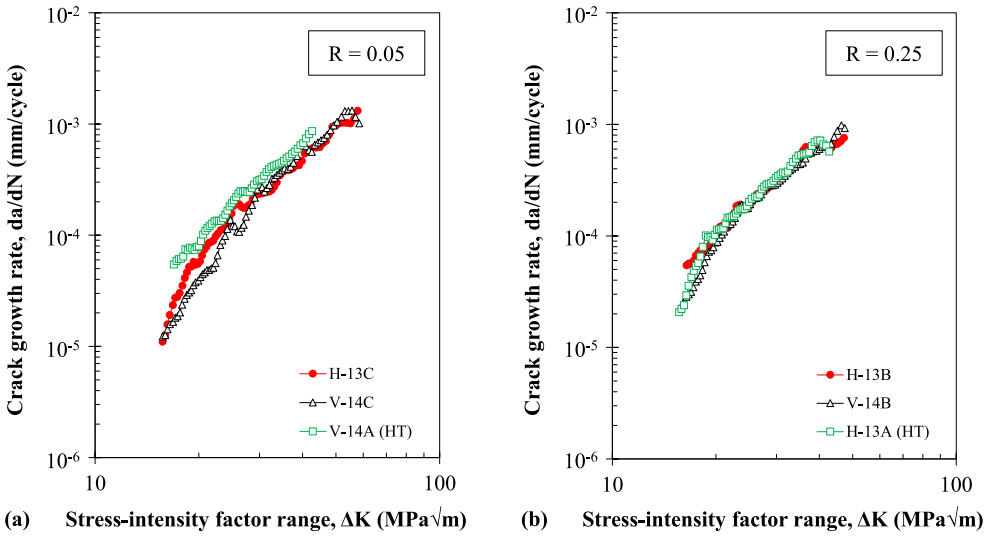

Fig. 6. Fatigue crack growth rate against stress-intensity factor range organised per stress range: (a) $R = 0.05$ and (b) $R = 0.25$.

Eq. (5) shows the relation between the fatigue crack opening ratio (U) and the stress-intensity factor range (ΔK), which indicates that ΔK_{eff} is the actual crack driving force when the crack remains open, being the dominant portion of fatigue life and is typically associated with the crack growth.

$$\Delta K_{eff} = U \bullet \Delta K \tag{5}$$

In this study, as explained in Section 2.5, the parameter U was determined for all R-ratios (0.05 and 0.25), loading orientations (horizontal and vertical) and material conditions (untreated and heat-treated). The differences in crack closure levels measured for each case are shown in Fig. 7. The most notable observation is the variation in crack closure levels for the different R-ratios studied. The average fatigue crack opening ratio for all specimens tested at $R = 0.05$ was 0.74, while for $R = 0.25$, the value was 0.94. This shows a stress ratio effect, with a higher crack closure effect for $R = 0.05$, as was also verified by Sales et al. [48] for WAAM super duplex stainless steels. This means the crack growth with a lower FCG rate for the test done at $R = 0.05$, as verified previously. On the other hand, the position and direction in which the specimens were obtained and the heat treatment did not significantly influence the crack closure level.

By eliminating the crack closure effect using Eq. (5), a figure displaying the FCG rates (da/dN) as a function of the effective stress-intensity factor range (ΔK_{eff}) can be constructed, as shown in Fig. 8. All series converge into a single curve in this representation, making it possible to trace a single potential fatigue crack growth rate (FCGR) law. This proves that the effect of the stress ratio on the different crack propagation rates is due to the varying levels of crack closure. Sales et al. [35] also reported collapsed curves when accounting for crack closure in WAAM super duplex stainless tested at stress ratios ranging from 0.01 to 0.5.

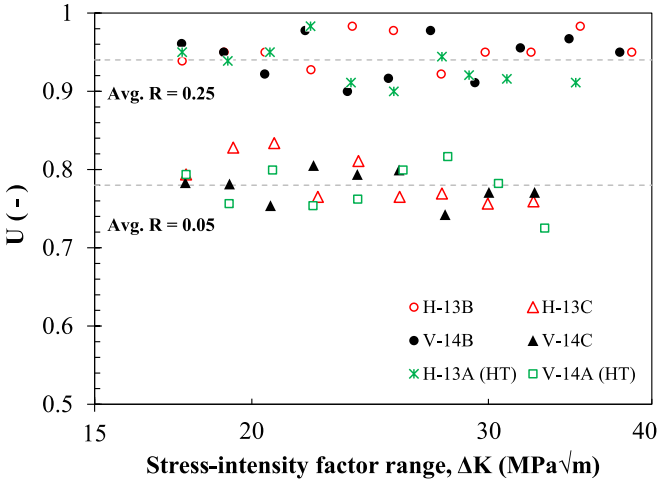

Fig. 7. Fatigue crack opening ratio, U, as a function of stress-intensity factor range.

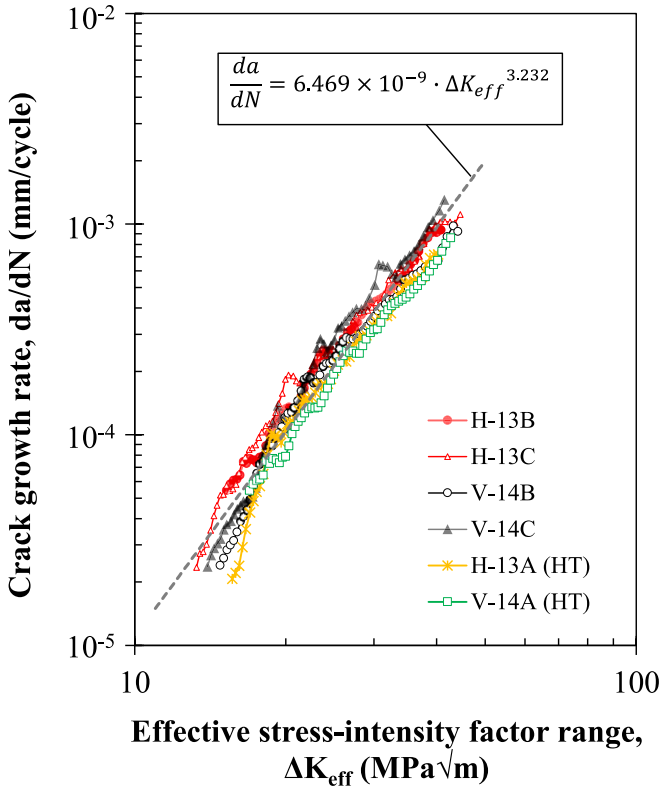

Fig. 8. FCG rates, da/dN, as a function of the effective stress-intensity factor range, ΔK_{eff}, for the untreated and heat-treated (HT) specimens cut horizontally (H) and vertically (V) to the printing direction.

3.4. Paris regime (da/dN-ΔK curves)

The microscopic propagation of the crack front in Regime II can be estimated by the Paris Law. In this second regime, the crack propagation rate increases linearly with the stress-intensity factor range, ΔK, and can be mathematically expressed as [49,50]:

$$\frac{da}{dN} = C(\Delta K)^m \tag{6}$$

where C and m are material constants that can be found through linear regression by plotting the $da/dN - \Delta K$ curves on a log–log scale. Expressed in a bi-logarithmic scale, Eq. (7) takes the form:

$$\log\left(\frac{da}{dN}\right) = \log C + m\log(\Delta K) \tag{7}$$

making it evident that the material constant m represents the slope of the crack growth rate curve. In this research, the fitting constants of the Paris Law were calculated by identifying the inflexion points that mark the transition between regimes and clearing the data sets from points belonging to Regimes I and III. The results are summarised in Table 5. The high values of the correlation coefficient, R^2, highlight the good agreement between the experimental results and the fitted constants.

The constant C depends on the microstructural properties of the material; for the same ΔK value, a higher C value indicates a higher fatigue crack propagation rate. The stress-intensity factor exponent, m, the slope of the curve, reflects the material's sensitivity to variations in the stress-intensity factor amplitude; a higher m value indicates faster fatigue crack propagation for small changes in ΔK. From Table 5, it can be seen that m values are within a range of 2 to 4, expected for wrought materials in the absence of a corrosive environment [51].

To illustrate the agreement of the tabulated values with the discussion thus far, consider the example of specimen V-14C, tested at $R = 0.05$, which displayed a slow propagation speed in Fig. 5(b) and Fig. 6(a). The slow propagation rate is supported by a low C value in comparison with other specimens, indicating high resistance to fatigue crack propagation. However, its m value also shows the highest sensitivity to variations in the stress-intensity factor range amongst the samples.

The Paris law constants calculated in this research were compared with other data sets from the literature for conventional S355 steel [52] and WAAM ER70S-6 steel [15,16,18]. Table 6 summarises the relevant fabrication and testing details, as well as the material constants for each one of these reference sources. Note that all the specimens had different thicknesses and were tested at different stress ratios compared to this research. Additionally, WAAM specimens vary in deposition strategy and orientation of the crack in relation to the printing direction. Nevertheless, the constant m does not differ significantly.

Fig. 9 compares the Paris law curves obtained in this study (in red for horizontal samples and black for vertical samples) with those compiled from the literature, as summarised in Table 6. Yellow [15], blue [16], and purple [18] lines represent results extracted from literature for WAAM ER70S-6, and the green lines display literature results for conventional S355 steel [52]. The Paris law curves proposed in this research closely align with those reported by previous authors for the same WAAM material [15,16,18], especially at higher stress-intensity factor range values ($\Delta K \geq 50$ MPa$\sqrt{\text{m}}$). Minor discrepancies are likely attributable to differences in the printing strategy, as previous studies have shown that the oscillatory pattern performs less effectively than the parallel pattern [18,53] and testing conditions.

Moreover, the FCGR curves derived in this study are consistent with results for conventional S355 steel [52], displaying similar slopes and falling within a reasonable range. However, S355 steel outperforms the different WAAM carbon steels analysed in this study, exhibiting lower fatigue crack propagation rates for equivalent stress-intensity factor ranges. These findings align with earlier studies' conclusions [15,18]. Furthermore, the results of this study also indicate that the print orientation did not significantly affect the material's FCG resistance, particularly at higher stress ratios, as evidenced by the near-identical dashed red and black lines of Fig. 9.

Fig. 9 shows that the recommendations of the standard BS 7910 for welded components [54], based on the two-stage FCG law (black solid lines), are appropriately conservative, reflecting the material's favourable FCG behaviour. Whereas the same two-stage FCG law for unwelded steel underestimates the FCG rates of the tested WAAM ER70S-6 carbon steel, highlighting the need for tailored guidelines to address the unique FCG characteristics of WAAM materials.

In summary, the FCG behaviour of the WAAM carbon steel from this research showed little sensitivity to variations in the loading direction relative to the print layer orientation, with other factors, such as stress ratio, exerting a more significant influence on the results. This last statement underscores the critical role of stress ratios in the fatigue response of components, along with the specimen's microstructure. This outcome is consistent with existing literature and applies to other metals, such as S355 steel referenced in this section [52]. Additionally, while S355 steel outperforms the analysed WAAM materials, the difference between them is not substantial, indicating the potential of WAAM carbon steel in the structural design of components. Finally, it can be concluded with high confidence that the applied heat treatment did not significantly enhance the mechanical properties.

Table 5
Paris law constants for the FCG tests on WAAM ER70S-6 carbon steel.

ID	Orientation	R	C	m	ΔK validity	R^2
H-13B	Horizontal	0.25	3.98×10^{-8}	2.63	$18.80 < \Delta K < 43.40$	0.98
H-13C	Horizontal	0.05	1.72×10^{-8}	2.79	$19.90 < \Delta K < 48.80$	0.98
V-14B	Vertical	0.25	3.97×10^{-8}	2.62	$19.70 < \Delta K < 47.40$	0.99
V-14C	Vertical	0.05	2.26×10^{-8}	3.36	$22.00 < \Delta K < 49.30$	0.96
H-13A (HT)	Horizontal	0.25	2.77×10^{-8}	2.76	$19.60 < \Delta K < 40.30$	1.00
V-14A (HT)	Vertical	0.05	2.17×10^{-8}	2.81	$19.70 < \Delta K < 48.30$	0.99

da/dN in mm/cycle and ΔK in MPa$\sqrt{\text{m}}$.

3.5. Fatigue crack growth mechanisms

Fig. 10 illustrates the fracture mechanics during fatigue crack propagation for two specimens with different orientations (vertical and horizontal) and tested at stress ratios of $R = 0.05$ and $R = 0.25$. The orange arrows at the bottom of the SEM micrograph illustrate the crack growth direction. It is possible to observe crushed asperity peaks caused by premature contact between crack faces during unloading due to crack closure (marked with red arrows). This contact influences crack opening in subsequent loading cycles, leading to local deformation and flattening of asperities. In Fig. 10(a), more of these regions can be visually identified compared to Fig. 10(b), as the specimens were tested under different stress ratios, with those tested at $R = 0.05$ exhibiting a higher level of crack closure.

Concerning the influence of the applied heat treatment, specimen location, and loading direction, no significant changes in the fatigue crack propagation mechanisms were perceptible through fractographic analysis. This suggests that the fatigue crack propagation behaviour in WAAM ER70S-6 carbon steel is not strongly affected by these variables, at least within the range of conditions tested in this research. The similar fracture patterns observed across the different specimens may indicate that the main factors influencing FCG behaviour in this additively manufactured steel are intrinsic to the material's microstructure and not associated with the external processing parameters studied.

The fracture mechanism observed in all specimens, regardless of the

Table 6
Comparative material constants for conventional S355 steel and WAAM ER70S-6 carbon steel.

Steel	Reference	Deposition strategy	Orientation	R	B(mm)	C	m
ER70S-6	Ermakova et al. [15]	Oscillatory	Horizontal	0.1	16	3.43×10^{-08}	2.61
	Ermakova et al. [15]	Oscillatory	Vertical	0.1	16	9.75×10^{-09}	2.95
	Shamir et al. [16]	Parallel	Horizontal	0.1	16	1.72×10^{-09}	3.42
	Shamir et al. [16]	Parallel	Vertical	0.1	16	1.13×10^{-08}	2.88
	Huang et al. [18]	Parallel	Diagonal	0.1	3	1.56×10^{-09}	3.38
	Huang et al. [18]	Parallel	Diagonal	0.1	8	2.88×10^{-09}	3.25
S355	Pedrosa et al. [52]	Conventional steel		0.1	12	7.27×10^{-10}	3.54
	Pedrosa et al. [52]	Conventional steel		0.5	12	1.63×10^{-08}	2.62

da/dN in mm/cycle and ΔK in MPa$\sqrt{m}$.

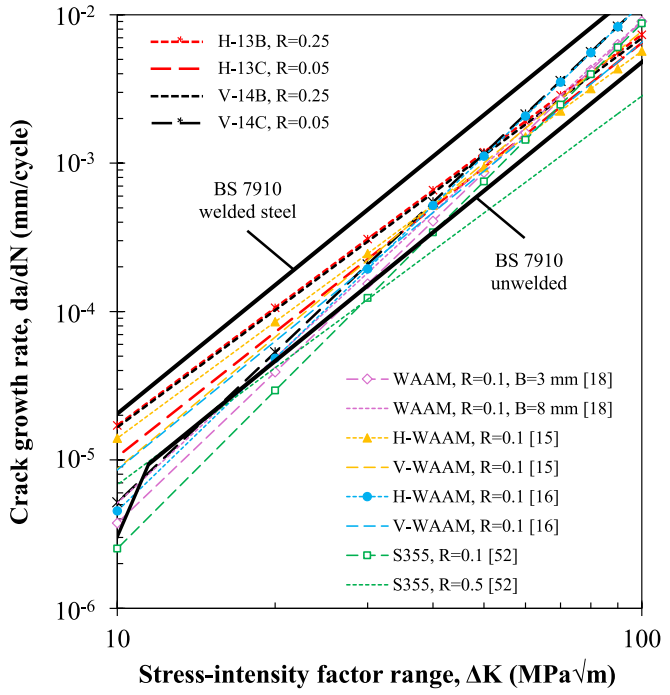

Fig. 9. Comparison of fitted experimental FCGR curves. Red and black dashed lines correspond to this research's specimens; purple [18], yellow [15], and blue [16] lines are for WAAM ER70S-6 extracted from literature, and green lines for conventional S355 steel [52], also extracted from literature; full black lines refer to two-stage FCG laws suggested by BS 7910 standard for welded and unwelded steel. (For interpretation of the references to colour in this figure legend, the reader is referred to the web version of this article.)

stress ratio, was a mix of cleavage and fatigue crack propagation striations caused by the loading cycle, as highlighted by red circles shown in the micrograph of Fig. 11 (the orange arrow marks the crack growth direction). Fatigue crack propagation striations exhibited variations in spacing and direction, likely influenced by localised microstructural changes and interaction with intersecting secondary cracks. However, fatigue crack propagation striations were mainly perpendicular to the crack growth direction. Cleavage fractures occur in the harder and more brittle regions, primarily composed of pearlite. In contrast, areas exhibiting striations, which are predominant, correspond to the softer and more ductile regions dominated by ferrite. Very small amounts of defects resulting from the manufacturing process were also observed. Fig. 11(b) shows two examples: a small inclusion and a porosity (marked by black arrows).

Previous studies have reported similar fractographic features in WAAM carbon steel for specimens subjected to different loading directions [18]. These main fractographic features included common fracture mechanisms associated with pearlite-ferrite steel, such as fatigue crack propagation striations, secondary cracks and dimples, which agrees with the present study's findings. In contrast, Ermakova et al. [15] concluded that microstructural deformation mechanisms in this additively manufactured steel are influenced by specimen orientation, with horizontal specimens exhibiting ductile failure and vertical specimens exhibiting brittle failure.

4. Conclusions

This paper studied the FCG behaviour of untreated and heat-treated WAAM ER70S-6 carbon steel under different stress ratios ($R = 0.05$ and $R = 0.25$) and loading directions (horizontal and vertical) relative to the layer printing orientation. Crack closure was measured via the DIC technique in combination with the incremental polynomial method. Microstructure and hardness were evaluated along three orthogonal planes for the various orientations and material conditions. Fracture surfaces were also examined to identify the fracture mechanisms of the Paris regime associated with the material condition and the printing orientation. FCG rates were compared with results from the literature for WAAM-produced and conventionally manufactured steels. The following conclusions can be drawn:

- The FCG behaviour of WAAM ER70S-6 carbon steel showed minimal sensitivity to variations in the loading direction relative to the print layer orientation. In contrast, factors such as the stress ratio had a more pronounced influence on the results. This highlights the critical role of stress ratio in the components' fatigue performance alongside the material's microstructure.
- The FCG rates closely aligned with existing literature for WAAM ER70S-6 carbon steel and were close to those of conventionally produced steel, such as S355 steel. S355 steel outperformed WAAM

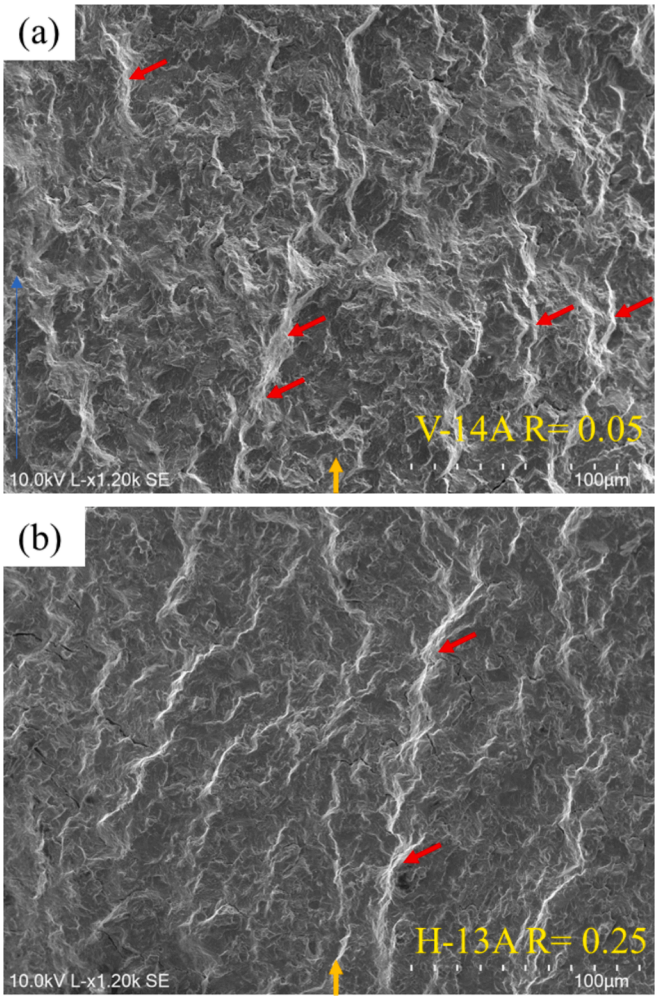

Fig. 10. Fracture mechanics during fatigue crack propagation. SEM micrograph of (a) V-14A specimen (HT) tested at $R = 0.05$ and (b) H-13A specimen (HT) tested at $R = 0.25$. SEM micrographs taken for $\Delta K = 30–35$ MPa$\sqrt{m}$. Orange arrow indicates the crack growth direction. (For interpretation of the references to colour in this figure legend, the reader is referred to the web version of this article.)

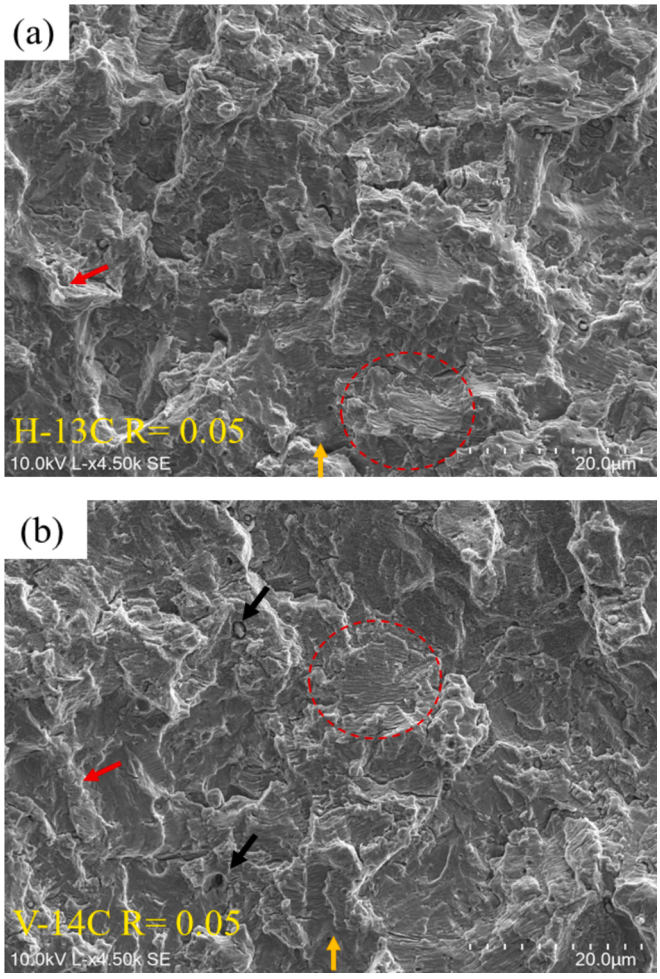

Fig. 11. Fracture mechanics during fatigue crack propagation stage. SEM micrograph of (a) H-13C specimen tested at $R = 0.05$ and (b) V-14C specimen tested at $R = 0.05$. SEM micrographs taken for $\Delta K = 30–35$ MPa$\sqrt{m}$. Orange arrow indicates the crack growth direction. (For interpretation of the references to colour in this figure legend, the reader is referred to the web version of this article.)

ER70S-6 carbon steel, but the difference was not significant, suggesting WAAM carbon steel's high potential for structural design.

- Annealing at 800 °C did not substantially enhance FCG rates, irrespective of the print layer orientation. This suggests that the microstructural changes induced by this heat treatment at this temperature were insufficient to improve fatigue resistance.
- The stress ratio significantly influenced the PICC mechanism, resulting in different FCG behaviours. Crack closure was more pronounced at $R = 0.05$, as evidenced by crushed asperity peaks caused by premature surface contact. This phenomenon may explain the variations in the fatigue life of structures produced using WAAM ER70S-6 carbon steel.
- Heat treatment, specimen location and loading orientation did not affect fatigue crack propagation mechanisms. The fractographic analysis revealed a mixed fracture mechanism in all cases, consisting of cleavage in the harder pearlite regions and fatigue crack propagation striations in the softer ferrite-dominant regions.
- No significant changes in fatigue crack propagation mechanisms were observed based on specimen location, loading orientation or material condition. Additionally, minor manufacturing defects, such as inclusions and porosity, were identified, potentially contributing to localised stress concentrations and crack initiation sites.

CRediT authorship contribution statement

Mariela Mendez-Morales: Writing – review & editing, Writing – original draft, Methodology, Investigation, Formal analysis, Conceptualization. **Joel S. Jesus:** Writing – review & editing, Validation, Supervision, Methodology, Investigation, Formal analysis, Conceptualization. **Ricardo Branco:** Writing – review & editing, Validation, Supervision, Methodology, Investigation, Formal analysis, Conceptualization. **Trayana Tankova:** Writing – review & editing, Supervision, Methodology, Conceptualization. **Carlos Rebelo:** Writing – review & editing, Supervision, Methodology, Funding acquisition, Conceptualization.

Declaration of competing interest

The authors declare that they have no known competing financial interests or personal relationships that could have appeared to influence the work reported in this paper.

Acknowledgements

i. This work was partly financed by FCT / MCTES through national funds (PIDDAC) under the R&D Unit Institute for Sustainability

and Innovation in Structural Engineering (ISISE), under reference UIDB/04029/2020 (doi.org/10.54499/UIDB/04029/2020), and under the Associate Laboratory Advanced Production and Intelligent Systems ARISE under reference LA/P/0112/2020.

ii. This research is sponsored by national funds through FCT – Fundação para a Ciência e a Tecnologia, under the project UIDB/00285/2020 and LA/P/0112/2020.

iii. This work is financed by national funds through FCT – Fundação para a Ciência e a Tecnologia, under grant agreement 2022.11645.BD attributed to the first author.

Data availability

Data will be made available on request.

References

[1] Ford S, Despeisse M. Additive manufacturing and sustainability: an exploratory study of the advantages and challenges. J Clean Prod 2016;137:1573–87. https://doi.org/10.1016/j.jclepro.2016.04.150.

[2] Huang R, Riddle M, Graziano D, Warren J, Das S, Nimbalkar S, et al. Energy and emissions saving potential of additive manufacturing: the case of lightweight aircraft components. J Clean Prod 2016;135:1559–70. https://doi.org/10.1016/j.jclepro.2015.04.109.

[3] Abdulhameed O, Al-Ahmari A, Ameen W, Mian SH. Additive manufacturing: challenges, trends, and applications. Adv Mech Eng 2019;11:1687814018822880. https://doi.org/10.1177/1687814018822880.

[4] Tankova T, da Silva LS. Robotics and additive manufacturing in the construction industry. Curr Robot Rep 2020;1:13–8. https://doi.org/10.1007/s43154-020-00003-8.

[5] Shah IH, Hadjipantelis N, Walter L, Myers RJ, Gardner L. Environmental life cycle assessment of wire arc additively manufactured steel structural components. J Clean Prod 2023;389:136071. https://doi.org/10.1016/j.jclepro.2023.136071.

[6] Webster GA, Behvar A, Shakil SI, Ribble R, Chou K, Krishnamurthy A, et al. Wire arc additive manufactured AWS ER100S-G steel: very high cycle fatigue characterization. Eng Fail Anal 2023;154:107721. https://doi.org/10.1016/j.engfailanal.2023.107721.

[7] Al-Nabulsi Z, Mottram JT, Gillie M, Kourra N, Williams MA. Mechanical and X ray computed tomography characterisation of a WAAM 3D printed steel plate for structural engineering applications. Constr Build Mater 2021;274:121700. https://doi.org/10.1016/j.conbuildmat.2020.121700.

[8] Webster GA, Ribble R, Chou K, Krishnamurthy A, Johnson E, Zekriardehani S, et al. Fatigue characterization of wire arc additive manufactured AWS ER100S-G steel: fully reversed condition. Eng Fail Anal 2023;153:107562. https://doi.org/10.1016/j.engfailanal.2023.107562.

[9] Gardner L. Metal additive manufacturing in structural engineering – review, advances, opportunities and outlook. Structures 2023;47:2178–93. https://doi.org/10.1016/j.istruc.2022.12.039.

[10] Kanyilmaz A, Demir AG, Chierici M, Berto F, Gardner L, Kandukuri SY, et al. Role of metal 3D printing to increase quality and resource-efficiency in the construction sector. Addit Manuf 2022;50:102541. https://doi.org/10.1016/j.addma.2021.102541.

[11] Xie Y, Gong M, Zhou Q, Li Q, Wang F, Zeng X, et al. Effect of microstructure on fatigue crack growth of wire arc additive manufactured Ti–6Al–4V. Mater Sci Eng A 2021;826:141942. https://doi.org/10.1016/j.msea.2021.141942.

[12] Kashaev N, Odermatt A, Vázquez L, Álvarez P. Fatigue life assessment of WAAM-processed Ti-6Al-4V. Proc Struct Integrity 2024;54:361–8. https://doi.org/10.1016/j.prostr.2024.01.094.

[13] Liao Z, Yang B, Xiao S, Yang G, Zhu T. Fatigue crack growth behaviour of an Al-Mg4.5Mn alloy fabricated by hybrid *in situ* rolled wire + arc additive manufacturing. Int J Fatigue 2021;151:106382. https://doi.org/10.1016/j.ijfatigue.2021.106382.

[14] Miao J, Chen J, Ting X, Hu W, Ren J, Li T, et al. Effect of solution treatment on porosity, tensile properties and fatigue resistance of Al–Cu alloy fabricated by wire arc additive manufacturing. J Mater Res Technol 2024;28:1864–74. https://doi.org/10.1016/j.jmrt.2023.12.114.

[15] Ermakova A, Mehmanparast A, Ganguly S, Razavi N, Berto F. Fatigue crack growth behaviour of wire and arc additively manufactured ER70S-6 low carbon steel components. Int J Fract 2022;235:47–59. https://doi.org/10.1007/s10704-021-00545-8.

[16] Shamir M, Igwemezie V, Lotfian S, Jones R, Asif H, Ganguly S, et al. Assessment of mechanical and fatigue crack growth properties of wire + arc additively manufactured mild steel components. Fatigue Fract Eng Mater Struct 2022;45:2978–89. https://doi.org/10.1111/ffe.13797.

[17] Ermakova A, Razavi N, Cabeza S, Gadalinska E, Reid M, Paradowska A, et al. The effect of surface treatment and orientation on fatigue crack growth rate and residual stress distribution of wire arc additively manufactured low carbon steel components. J Mater Res Technol 2023;24:2988–3004. https://doi.org/10.1016/j.jmrt.2023.03.227.

[18] Huang C, Zheng Y, Chen T, Ghafoori E, Gardner L. Fatigue crack growth behaviour of wire arc additively manufactured steels. Int J Fatigue 2023;173:107705. https://doi.org/10.1016/j.ijfatigue.2023.107705.

[19] Wolf E. Fatigue crack closure under cyclic tension. Eng Fract Mech 1970;2:37–45. https://doi.org/10.1016/0013-7944(70)90028-7.

[20] Hughes JM, Wallbrink C, Kotousov A. Cycle-by-cycle crack closure measurements and fatigue crack growth in CT specimen made of 7075-T7351 aluminium. Proc Struct Integrity 2023;45:44–51. https://doi.org/10.1016/j.prostr.2023.05.012.

[21] Newman JC, Kota K, Lacy TE. Fatigue and crack-growth behavior in a titanium alloy under constant-amplitude and spectrum loading. Eng Fract Mech 2018;187:211–24. https://doi.org/10.1016/j.engfracmech.2017.10.036.

[22] Vidler J, Kotousov A, Ng C-T. Compliance changes for a fatigue edge crack. Eur J Mech A Solids 2025;111:105592. https://doi.org/10.1016/j.euromechsol.2025.105592.

[23] Tomar B, Shiva S, Nath T. A review on wire arc additive manufacturing: processing parameters, defects, quality improvement and recent advances. Mater Today Commun 2022;31:103739. https://doi.org/10.1016/j.mtcomm.2022.103739.

[24] Agnani M, Findley KO, Thompson SW. Effects of retained austenite and martensite microstructure on fatigue crack propagation in quenched and tempered high carbon steels. Int J Fatigue 2024;188:108529. https://doi.org/10.1016/j.ijfatigue.2024.108529.

[25] AWS. AWS A5.18/A5.18M:2005 Specification for carbon steel electrodes and rods for gas shielded arc welding; 2005.

[26] Electro-Portugal. EUROTROD Welding Consumables 2015. http://www.electroportugal.com/downloads/file70_pt.pdf.

[27] Tankova T, Andrade D, Branco R, Zhu C, Rodrigues D, Simões da Silva L. Characterization of robotized CMT-WAAM carbon steel. J Constr Steel Res 2022;199:107624. https://doi.org/10.1016/J.JCSR.2022.107624.

[28] Mendez-Morales M, Branco R, Tankova T, Rebelo C. Assessment of cyclic deformation behaviour of wire arc additively manufactured carbon steel. Int J Fatigue 2024;184:108307. https://doi.org/10.1016/j.ijfatigue.2024.108307.

[29] ASTM. ASTM E647-24 Standard test method for measurement of fatigue crack growth rates 2024.

[30] Vahedi Nemani A, Ghaffari M, Nasiri A. Comparison of microstructural characteristics and mechanical properties of shipbuilding steel plates fabricated by conventional rolling versus wire arc additive manufacturing. Addit Manuf 2020;32:101086. https://doi.org/10.1016/j.addma.2020.101086.

[31] ASTM. ASTM E3-11 Standard guide for preparation of metallographic specimens 2017.

[32] ASTM. ASTM E384-22 Standard test method for microindentation hardness of materials 2022.

[33] Jesus JS, Borrego LP, Ferreira JAM, Branco R, Costa JD, Capela C. Fatigue crack growth under mixed mode I + II in Ti-6Al-4V specimens produced by Laser powder Bed fusion. Eng Fract Mech 2022;264:108327. https://doi.org/10.1016/j.engfracmech.2022.108327.

[34] Iliopoulos A, Michopoulos JG. On the feasibility of crack propagation tracking and full field strain imaging via a strain compatibility functional and the Direct Strain Imaging method. Int J Impact Eng 2016;87:186–97. https://doi.org/10.1016/j.ijimpeng.2015.03.006.

[35] DVDVideoSoft Ltd. DVDVideoSoft [Computer software]. London, UK: DVDVideoSoft Ltd; 2024.

[36] Co AIE. GOM Correlate [Computer software]. Hanoi, Vietnam: AIE Co; 2020.

[37] Fernandes RF, Jesus JS, Borrego LP, Ferreira JAM, Branco R, Costa JD, et al. Failure analysis of fatigue crack propagation in specimens of AlSi10Mg aluminum alloy produced by L-PBF: Effect of different heat treatments. Eng Fail Anal 2024;163:108595. https://doi.org/10.1016/j.engfailanal.2024.108595.

[38] Allison JE, Ku RC, Pompetzki MA. A comparison of measurement methods and numerical procedures for the experimental characterization of fatigue crack closure; 1988. doi: 10.1520/STP27207S.

[39] Jesus JS, Borrego LP, Ferreira JAM, Costa JD, Capela C. Fatigue crack growth behaviour in Ti6Al4V alloy specimens produced by selective laser melting. Int J Fract 2020;223:123–33. https://doi.org/10.1007/s10704-019-00417-2.

[40] Aprilia A, Zhai W, Guo Y, Aishwarya SR, Zhou W. Decarburization of wire-arc additively manufactured ER70S-6 steel. Materials 2023;16:3635. https://doi.org/10.3390/ma16103635.

[41] Ermakova A, Mehmanparast A, Ganguly S, Razavi N, Berto F. Investigation of mechanical and fracture properties of wire and arc additively manufactured low carbon steel components. Theor Appl Fract Mech 2020;109:102685. https://doi.org/10.1016/j.tafmec.2020.102685.

[42] Dantas R, Correia J, Lesiuk G, Rozumek D, Zhu S-P, de Jesus A, et al. Evaluation of multiaxial high-cycle fatigue criteria under proportional loading for S355 steel. Eng Fail Anal 2021;120:105037. https://doi.org/10.1016/j.engfailanal.2020.105037.

[43] Kujawski D, Ellyin F. A fatigue crack growth model with load ratio effects. Eng Fract Mech 1987;28:367–78. https://doi.org/10.1016/0013-7944(87)90182-2.

[44] Xin H, Correia JAFO, Veljkovic M. Three-dimensional fatigue crack propagation simulation using extended finite element methods for steel grades S355 and S690 considering mean stress effects. Eng Struct 2021;227:111414. https://doi.org/10.1016/j.engstruct.2020.111414.

[45] Ramirez J, Potirniche GP, Shaber N, Stephens R, Charit I. Experimental and computational studies of load ratio effect on fatigue crack growth rates in Alloy 709 at elevated temperatures. Fatigue Fract Eng Mater Struct 2023;46:3596–609. https://doi.org/10.1111/ffe.14089.

[46] Zhang J, Wang X, Paddea S, Zhang X. Fatigue crack propagation behaviour in wire +arc additive manufactured Ti-6Al-4V: effects of microstructure and residual

stress. Mater Des 2016;90:551–61. https://doi.org/10.1016/j.matdes.2015.10.141.
[47] Zhang X, Martina F, Ding J, Wang X, Williams SW. Fracture toughness and fatigue crack growth rate properties in wire + arc additive manufactured Ti-6Al-4V. Fatigue Fract Eng Mater Struct 2017;40:790–803. https://doi.org/10.1111/ffe.12547.
[48] Sales A, Khanna A, Hughes J, Yin L, Kotousov A. Fatigue crack growth rates and crack tip opening loads in CT specimens made of SDSS and manufactured using WAAM. Materials 2024;17:1842. https://doi.org/10.3390/ma17081842.
[49] Paris P, Erdogan F. A critical analysis of crack propagation laws. J Basic Eng 1963;85:528–33. https://doi.org/10.1115/1.3656900.
[50] Paris PC, Gomez MP, Anderson WE. A rational analytic theory of fatigue. Trend Eng 1961;13:9–14.
[51] Anderson TL. In: Fracture mechanics: fundamentals and applications. 4th ed. Boca Raton: CRC Press; 2017. https://doi.org/10.1201/9781315370293.
[52] Pedrosa B, Correia J, Lesiuk G, Rebelo C, Veljkovic M. Fatigue crack growth modelling for S355 structural steel considering plasticity-induced crack-closure by means of UniGrow model. Int J Fatigue 2022;164:107120. https://doi.org/10.1016/j.ijfatigue.2022.107120.
[53] Wang Z, Hou Y, Huang C, Han Q, Zong L, Chen M-T, et al. Experimental study and constitutive modelling of wire arc additively manufactured steel under cyclic loading. J Constr Steel Res 2024;213:108420. https://doi.org/10.1016/j.jcsr.2023.108420.
[54] BSI. BS 7910:2013+A1:2015 Guide to methods for assessing the acceptability of flaws in metallic structures 2015.